Nano-Micro Letters
e-ISSN 2150-5551
CN 31-2103/TB
ARTICLE
https://doi.org/10.1007/s40820-023-01063-z

Cite as
Nano-Micro Lett.
(2023) 15:94

Received: 21 December 2022
Accepted: 2 March 2023
Published online: 10 April 2023

Self-Supporting Nanoporous Copper Film with High Porosity and Broadband Light Absorption for Efficient Solar Steam Generation

Bin Yu[1], Yan Wang[2], Ying Zhang[1], Zhonghua Zhang[1] ✉

HIGHLIGHTS

- Self-supporting Cu film with high porosity was obtained by dealloying of $Al_{98}Cu_2$.
- Nanoporous Cu (NP-Cu) film shows good hydrophilicity and strong broadband light absorption.
- NP-Cu film exhibits outstanding solar steam generation and desalination performance.

ABSTRACT Solar steam generation (SSG) is a potential technology for freshwater production, which is expected to address the global water shortage problem. Some noble metals with good photothermal conversion performance have received wide concerns in SSG, while high cost limits their practical applications for water purification. Herein, a self-supporting nanoporous copper (NP-Cu) film was fabricated by one-step dealloying of a specially designed $Al_{98}Cu_2$ precursor with a dilute solid solution structure. In-situ and ex-situ characterizations were performed to reveal the phase and microstructure evolutions during dealloying. The NP-Cu film shows a unique three-dimensional bicontinuous ligament-channel structure with high porosity (94.8%), multi scale-channels and nanoscale ligaments (24.2 ± 4.4 nm), leading to its strong broadband absorption over the 200–2500 nm wavelength More importantly, the NP-Cu film exhibits excellent SSG performance with high evaporation rate, superior efficiency and good stability. The strong desalination ability of NP-Cu also manifests its potential applications in seawater desalination. The related mechanism has been rationalized based upon the nanoporous network, localized surface plasmon resonance effect and hydrophilicity.

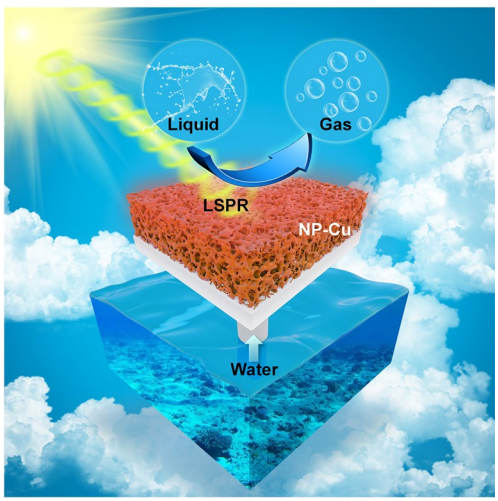

KEYWORDS Solar steam generation; Nanoporous copper; Broadband solar absorption; Localized surface plasmon resonance; Seawater desalination; Dealloying

1 Introduction

The shortage of freshwater resources has currently become one of the main threats to the sustainable development of human society. Unfortunately, all forms of freshwater resources are merely 2.5% of the total global water [1]. Therefore, saline water utilization is one of the important ways to solve the global freshwater shortage and has become a long-term development strategy of many countries [2]. To this end, a lot of efforts have been made to obtain clean drinking water from seawater or

✉ Zhonghua Zhang, zh_zhang@sdu.edu.cn
[1] Key Laboratory for Liquid-Solid Structural Evolution and Processing of Materials (Ministry of Education), School of Materials Science and Engineering, Shandong University, Jingshi Road 17923, Jinan 250061, People's Republic of China
[2] School of Materials Science and Engineering, University of Jinan, West Road of Nan Xinzhuang 336, Jinan 250022, People's Republic of China

wastewater [3–8]. Some traditional desalination methods (such as multistage flash distillation [9] and reverse osmosis [10]) require a lot of energy [11] and pollutants generated by burning fossil fuels have a negative impact on the environment [12]. Other desalination methods such as electrodialysis and emerging capacitive deionization, which are not suitable for seawater with high salt concentrations [13, 14]. So solar steam generation (SSG) using solar energy to desalinate seawater has been considered as one of the most attractive desalination technologies [15, 16]. The SSG technology does not need any moving parts and high-pressure operation [17], which with strong expansibility is easy to be coupled with other technologies to realize multi-function such as power generation, medical sterilization and wastewater purification [18–21].

Efficient SSG systems need to meet the following characteristics: excellent photothermal conversion capability, reasonable heat management, and efficient water transportation and evaporation. Photothermal materials with excellent solar absorption and photothermal conversion capacities are the basis to ensure efficient SSG [22]. Over the past decade, many SSG systems have been developed based on different types of photothermal materials, such as metals [23–25], semiconductors [26–28], polymers [29–31], biomass carbon materials [32–34], MXenes [35], and graphenes [36–38]. Among them, plasmonic metal nanomaterials (Au [39–41], Ag [42–44], Pd [45, 46], Pt [47, 48], etc.) have aroused extensive attention due to their localized surface plasmon resonance (LSPR) property. Compared with other photothermal materials, plasmonic metal nanomaterials have the advantages of easy control of optical properties and structure, adjustable heat radiation loss, abundant optional types and good mechanical stability [49, 50]. However, the cost and practicability of noble metals hinder their further applications in SSG. Hence, developing non-noble metal-based photothermal materials is of central importance to achieve efficient and durable SSG [51].

Photothermal materials have good hydrophilicity and sufficient porous structure by constructing hierarchical nano/microstructures, which is an important guarantee for high-efficiency sunlight absorption, water transfer and steam escape [52]. Traditional metal-based photothermal films are obtained by depositing metal nanoparticles onto porous substrates (such as airlaid paper, wood, filter paper and carbon cloth) [42]. It would be better to construct metal-based photothermal films with a porous structure and self-supporting morphology. Dealloying during which the more noble element diffuses and reorganizes into a three-dimensional (3D) bicontinuous ligament/channel structure with the selective removal of the less noble element, has been widely used to prepare nanoporous metals [53, 54]. This provides an idea for preparing self-supporting porous metal-based photothermal films. For example, Zhang et al. [39] reported a dealloying-driven black gold film with a hierarchically porous structure and good SSG performance. Cu is a potential candidate for photothermal materials because of its good plasmonic properties and low cost [55]. Nanoscale Cu is a typical plasmonic metal and the potential application of Cu in SSG has been explored [56–59]. However, nanoporous Cu (NP-Cu) films fabricated by dealloying have received less attention in SSG.

Herein, we demonstrated a one-step dealloying strategy to fabricate a self-supporting NP-Cu film with high porosity and light weight. A dilute solid solution alloy ($Al_{98}Cu_2$, at%) was elaborately designed for dealloying, and the involved microstructural evolutions were probed by in-situ and ex-situ characterization methods. The obtained NP-Cu film with the porosity of 94.8% and density of 0.4679 g cm^{-3} shows excellent broadband light absorption of 200–2500 nm in wavelength and outstanding SSG performance.

2 Experimental

2.1 Materials Preparation

The $Al_{98}Cu_2$ ingot was prepared by co-melting Al and Cu (99.99 wt% purity) in a sealed quartz tube filled with argon using high-frequency induction heating. Then the ingot was cold-rolled to a sheet with a thickness of around 300 μm. Afterwards, the sheet was annealed at 550 °C for 300 min in vacuum and then immediately quenched in water. Eventually, the as-quenched $Al_{98}Cu_2$ sheet was dealloyed in a 0.5 M NaOH aqueous solution until no gas bubbles evolved at room temperature, and the self-supporting NP-Cu film was obtained. The dealloying process usually lasted for about 11 h. Additionally, the NP-Cu film was annealed in an argon-hydrogen atmosphere at 500 °C for 120 min to prepare the coarsened sample (named as NP-Cu-500).

2.2 Materials Characterization

The phase compositions of all samples were probed by X-ray diffraction (XRD, XD-3) with Cu Kα radiation.

https://doi.org/10.1007/s40820-023-01063-z

The microstructures and chemical compositions of the as-dealloyed samples were characterized by transmission electron microscopy (TEM, FEI Titan 80–300) and scanning electron microscopy (SEM, JSM-7800F) equipped with an energy dispersive X-ray (EDX) analyzer. Electron backscattering diffraction (EBSD) analysis of the $Al_{98}Cu_2$ precursor was also performed using SEM. X-ray photoelectron spectroscopy (XPS) was used to characterize the chemical states of elements in the dealloyed samples using an AXIS Supra spectrometer with Al Kα exciting source. All XPS spectra were calibrated by C 1*s* with the binding energy at 284.6 eV. Absorption spectra of the NP-Cu/NP-Cu-500 films were recorded by employing an ultraviolet-visible-near-infrared (UV-vis-NIR) spectrophotometer (UV-3600, Shimadzu) equipped with an integrating sphere. The infrared reflection spectrum of the NP-Cu film was measured by a Fourier transform infrared (FTIR) spectrometer (Nicolet iS50). The thermal conductivities were measured by a hot disk method (Hot Disk TPS 2500S). The DSA100S goniometer was used to measure the contact angle. In addition, in-situ XRD and ex-situ SEM were conducted to explore the phase and microstructure evolutions of the $Al_{98}Cu_2$ precursor during dealloying.

2.3 SSG and Desalination Experiments

Figure S1 shows the SSG setup. A solar simulator (PLS-SXE300/300UV) with an AM 1.5G filter was used as the light source. An optical power meter (PL-MW2000) was used to detect the light intensity. Infrared images and the corresponding temperatures were recorded by an IR camera (FLIR E8xt). The real-time mass change of water was recorded by an electronic balance (BSA124S-CW, Sartorius). A SSG system with a wick structure was used to test the water evaporation capacity of the NP-Cu samples. The samples were placed on a polystyrene (PS) foam, and a cotton pillar was used as a channel to supply water. The SSG tests were performed at 28 °C and relative humidity of about 40%. Additionally, the desalination ability of NP-Cu was tested using natural seawater from Bohai Sea, South China Sea and Yellow Sea. The ion concentrations in the seawater and the collected clean water were determined by inductively coupled plasma mass spectrometer (ICP-MS, Agilent 7700).

3 Results and Discussion

3.1 Fabrication and Structural Characterization of NP-Cu Films

According to the phase diagram of Al-Cu (Fig. 1a) [60, 61], the composition point of the precursor was set as 2 at%. The annealing and quenching treatments could ensure the formation of solid solution in the $Al_{98}Cu_2$ precursor. The EBSD image (Fig. 1b and inset) clearly reveals the size (several hundred microns), shape and crystallographic orientations of equiaxed grains in the $Al_{98}Cu_2$ precursor. Due to the minor content of Cu in $Al_{98}Cu_2$, Cu atoms can occupy the lattice sites of Al to form the dilute Al(Cu) solid solution (Fig. 1c). As shown in Fig. S2, the as-rolled $Al_{98}Cu_2$ precursor is composed of Al phase (PDF# 04-0787) and minor Al_2Cu phase (PDF# 02-1309). In comparison, the as-annealed sample only consists of a single Al phase (Fig. 1d), indicating the formation of Al(Cu) solid solution. After dealloying, the XRD pattern of the NP-Cu film (Fig. 1d) only shows three broad peaks (at $2\theta = 43.3°$, 50.4° and 74.1°) of the Cu phase (PDF# 04-0836), indicating the thorough dealloying of $Al_{98}Cu_2$ in the NaOH solution. The EDX results (Fig. S3) further confirm that most of Al was selectively etched away during dealloying and the residual Al amount is only 1.3 at%. Moreover, the color of the sample changed from silvery white ($Al_{98}Cu_2$) to black (NP-Cu) after dealloying, but its self-supporting characteristic is well retained (inset of Fig. 4d).

The microstructural evolution of the $Al_{98}Cu_2$ precursor during dealloying was further explored by ex-situ SEM (Figs. 2 and S4). After 1 min of dealloying, the surface of $Al_{98}Cu_2$ was slightly corroded (Fig. S4a) and island-like humps formed (Fig. S4b). Notably, some irregular second-phase (Al_2Cu) particles appeared inside corrosion pits along the grain boundaries (Fig. S4c, d), but could not be detected by XRD (Fig. 1d). After 3 min of dealloying, bubbles-induced pits emerged on the sample surface and the bicontinuous ligament-channel structure could be clearly observed (Fig. 2a, b). Moreover, the corrosion degree of the grain boundaries deepened (Fig. 2c, d). The grains and grain boundaries became more obvious with increasing dealloying time to 5 min (Fig. 2e, f). Furthermore, different grains showed distinct corrosion characteristics (Fig. 2g, h). Notably, some grain surfaces appear fibrous

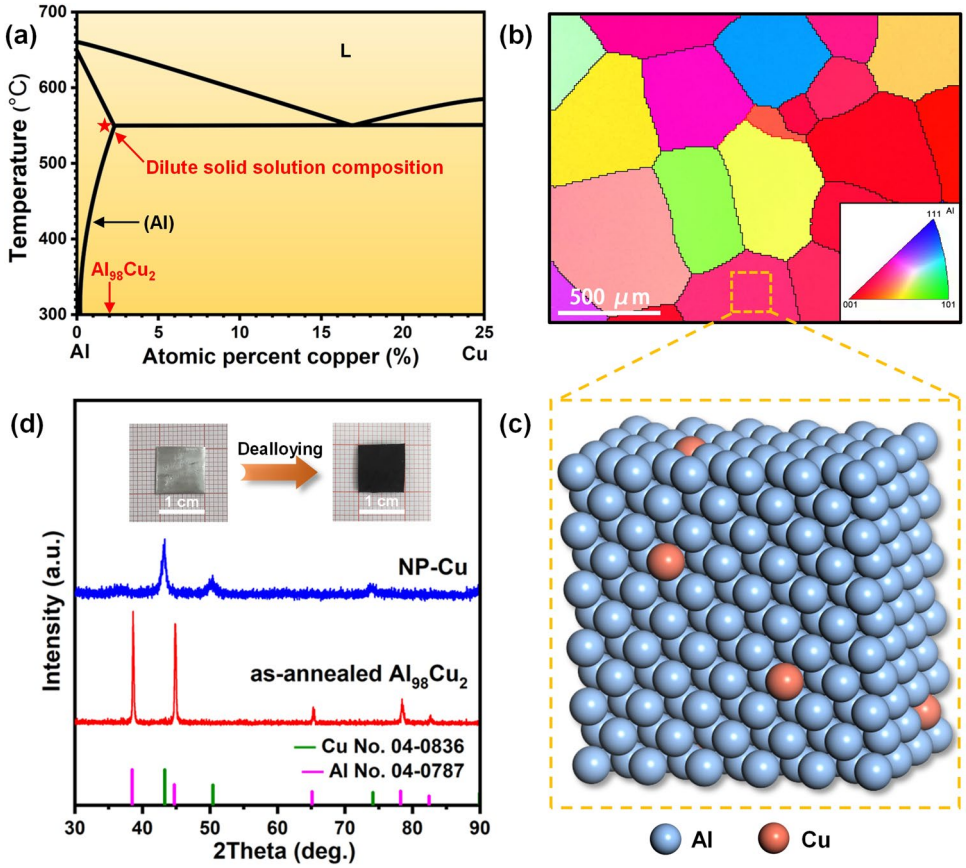

Fig. 1 **a** Phase diagram of Al-Cu indicating the design of dilute solid solution alloy. **b** EBSD image (Inset: corresponding crystallographic orientation) and **c** schematic diagram of the crystal structure of the $Al_{98}Cu_2$ precursor. **d** XRD patterns (Inset: photographs of the samples before and after dealloying) of the as-annealed $Al_{98}Cu_2$ precursor and the NP-Cu film

structures after 5 min of dealloying (Fig. 2e–g), probably due to different orientations of the grains (Fig. 1b). With the extension of dealloying time, the surface corrosion further deepened, and the nanoporous structure became more obvious (Fig. S4e–h). After 20 min of dealloying (Fig. 2i), the grain shape and size of the dealloyed surface are similar to those in the precursor (Fig. 1b), and the second phase at the grain boundaries disappeared owing to the dealloying of Al_2Cu (Fig. 2j–l). When dealloying for 60 min, farmland-like cracks appeared inside the grains (Fig. S4i–l). After 120 min of dealloying, both interlaced and parallel cracks appeared in different grains, and the ligament-channel structure could be observed in the porous layer (Fig. 2m–p). The photographs in Fig. S5 show the gradual blackening of the surface of the dealloyed samples. Figure 2q vividly demonstrates the structural characteristics and evolution of different dealloying stages.

In-situ XRD was further performed to explore the phase evolution during dealloying of $Al_{98}Cu_2$ (Fig. 3a, b). Figure 3a shows that the peak intensity of Al(Cu) gradually decreases with the prolongation of the dealloying time. The broad diffraction peak of Cu (111) begins to appear after 300 min of dealloying and gradually becomes stronger. Thereafter, the other two diffraction peaks of Cu (200) and (220) can be observed, whose intensities further increase with dealloying time. But their peak positions do not change with time, and are consistent with standard values of *f.c.c.* Cu. And no intermediate phase emerges during the whole dealloying process. Finally, only Cu peaks remain in the XRD pattern. The corresponding contour plot in Fig. 3b visually shows the phase evolution and involved strength/position changes of diffraction peaks with the dealloying time. Figure 3c shows the macroscopic morphology/color change of $Al_{98}Cu_2$ during dealloying. Violent H_2 bubbles

 https://doi.org/10.1007/s40820-023-01063-z

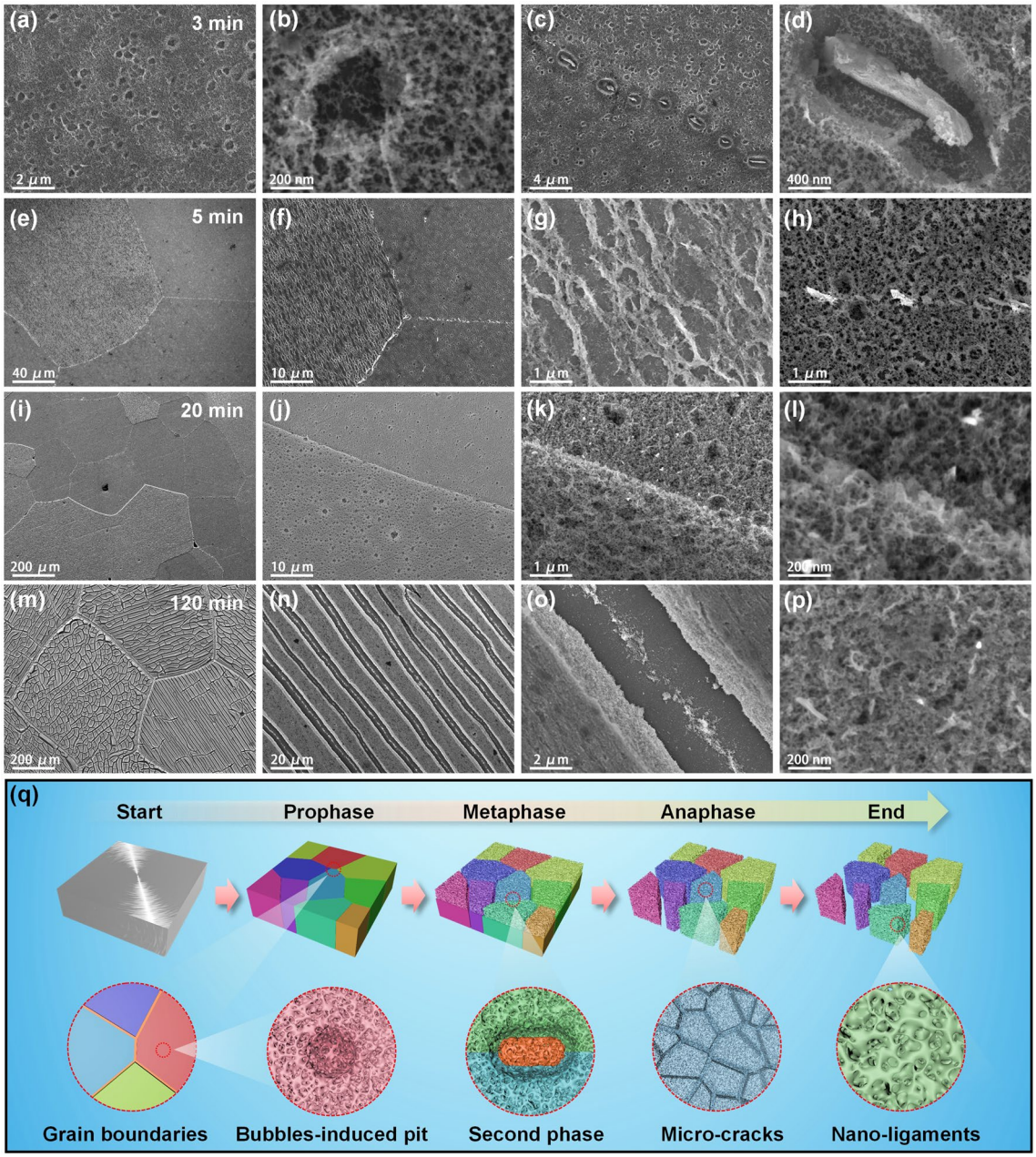

Fig. 2 Plan-view SEM images of $Al_{98}Cu_2$ dealloyed for (**a–d**) 3, (**e–h**) 5, (**i–l**) 20, and (**m–p**) 120 min in the 0.5 M NaOH solution. **q** Schematic illustrations showing the microstructure evolution of $Al_{98}Cu_2$ during dealloying

formed due to the reaction of Al with NaOH before 9 h of dealloying. Subsequently, the bubbles obviously decreased and finally disappeared at the dealloying of 11 h. And the color of the sample became dark and black. In addition, after 10.5 h of dealloying, an evident area shrinkage ($\Delta S/S_0$) could be observed, and the final area shrinkage is around 14%.

The composition and valence state of the $Al_{98}Cu_2$ samples dealloyed for 3 and 10 min were further determined by XPS. Two peaks located at 932.4 and 952.3 eV of Cu 2*p* spectra (Fig. 3d) can be assigned to the Cu $2p_{3/2}$ and Cu $2p_{1/2}$ signals, respectively, illustrating the existence of the metallic state (Cu^0) [62, 63]. Meanwhile, the peak of Cu^{2+} in CuO and its shake-up satellite peak can be observed

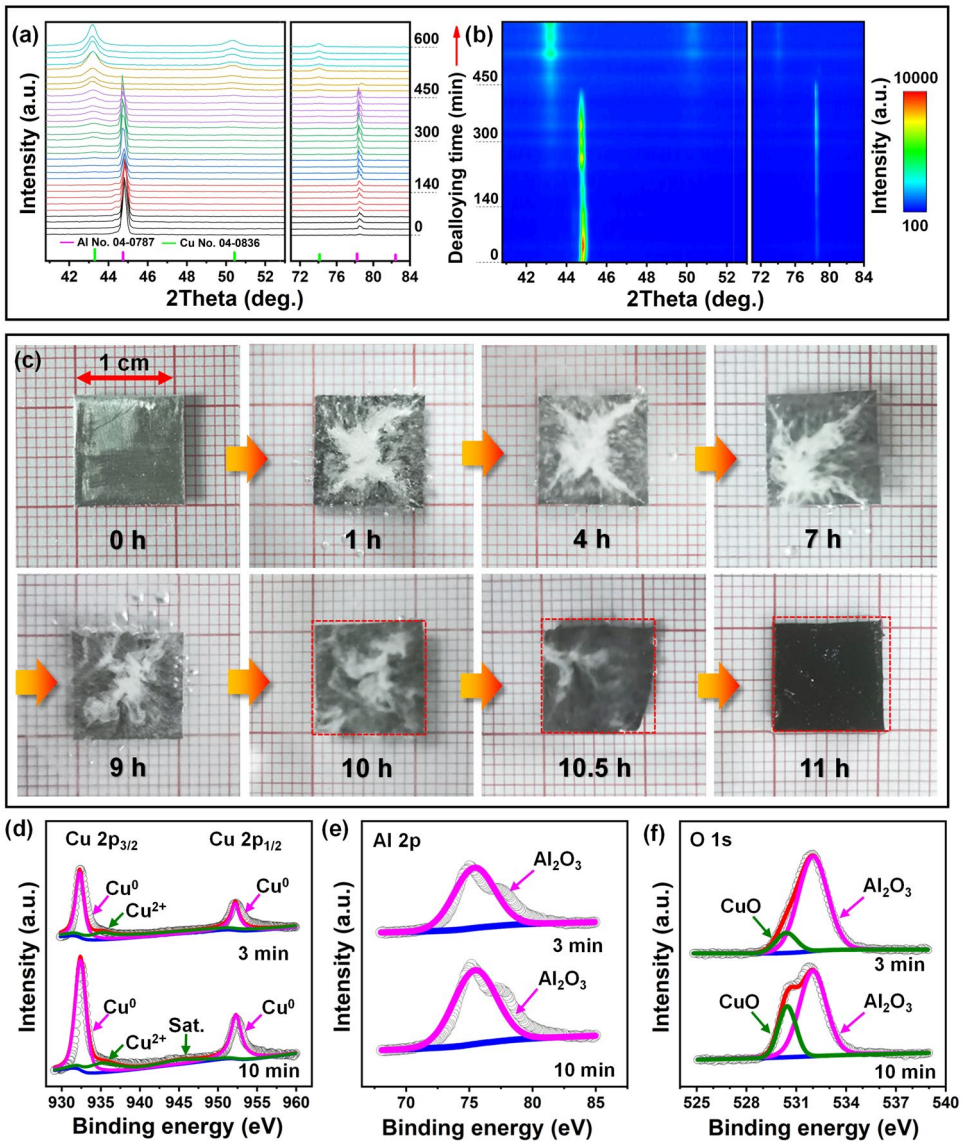

Fig. 3 **a** In-situ XRD patterns and **b** corresponding contour plot showing the phase evolution of the $Al_{98}Cu_2$ precursor during dealloying in the 0.5 M NaOH solution. **c** Macrophotographs of the $Al_{98}Cu_2$ alloy foil dealloyed for different durations. The red dashed boxes represent the size of the pristine precursor. XPS spectra of **d** Cu 2*p*, **e** Al 2*p* and **f** O 1*s* of the $Al_{98}Cu_2$ foils dealloyed for 3 and 10 min

at 935.4 and 945.0 eV, respectively, indicating the slight surface oxidation. When the dealloying time was extended from 3 to 10 min, the peak intensity of Cu^0 increases obviously. This is because Al atoms on the surface of $Al_{98}Cu_2$ were constantly corroded away and the nanoporous structure composed of Cu formed. The Al 2*p* spectra (Fig. 3e) show a characteristic peak at 75.4 eV, indicating the presence of Al^{3+} (Al_2O_3) [64]. The peak intensity of Al 2*p* has no obvious change for these two samples. Additionally, the O 1*s* peaks are composed of two components (Fig. 3f). The two peaks at 530.4 [63] and 532.0 [65, 66] eV correspond to CuO and Al_2O_3, respectively. Compared with the scenario of 3 min of dealloying, the peak intensity associated with CuO is significantly enhanced at dealloying for 10 min, which is related to the increase of Cu content on the sample surface.

The obtained NP-Cu film was further characterized by SEM and TEM (Figs. 4a–g and S6). The SEM images in Figs. 4a, b and S6a show the river bed-like morphology of the NP-Cu film surface, which displays numerous channels with tens of microns in width. The cross-sectional SEM

 https://doi.org/10.1007/s40820-023-01063-z

images in Figs. 4c and S6d–f show that the channels run through the whole section of NP-Cu and can serve as effective paths for water transport. Figure 4d displays a typical 3D bicontinuous ligament-channel structure of the NP-Cu film with the average ligament size of 21.9 ± 3.6 nm (Fig. S7a). The representative TEM images (Fig. 4e, f) reveal the typical nanoporous structure of NP-Cu, and nanoscale pores/ligaments can be visualized. The selected-area electron diffraction (SAED) pattern of NP-Cu (inset of Fig. 4e) reveals polycrystalline rings which can be indexed as (111), (200), (220) and (311) planes of the *f.c.c.* Cu (in agreement with the XRD result in Fig. 1d). Figure 4g illustrates the high-resolution TEM (HRTEM) image with lattice fringes of Cu (111). Based on the TEM results, the average ligament size of NP-Cu was further determined to be 24.2 ± 4.4 nm (Fig. 4h). Noticeably, the NP-Cu film possesses an ultrahigh porosity of 94.8% (Section S2), which is caused by a large number of microscale channels and nanoscale pores produced by the dealloying of the dilute solid solution $Al_{98}Cu_2$ (Fig. 4i). The volume shrinkage is about 59.4%, which is compatible with the obvious area shrinkage and huge thickness shrinkage (Figs. 3c and S7b). In addition, the density of the NP-Cu film is only 0.4679 g cm^{-3}, much lower than that of bulk Cu (8.960 g cm^{-3}).

XPS was applied to further analyze the chemical valences of the NP-Cu film (Figs. 4j and S8) and the $Al_{98}Cu_2$ precursor (Fig. S9). In the NP-Cu film, the binding energies at 932.2 and 952.1 eV are assigned to Cu^0, while the peaks located at 935.2 and 945.0 eV are attributed to the Cu^{2+} and corresponding satellite peak, respectively (Fig. 4j) [62, 63]. The weak peaks of Cu^{2+} indicate that the NP-Cu film was slightly oxidized. However, the signal of Cu 2*p* in the $Al_{98}Cu_2$ precursor is weak, and only weak peaks of Cu^0 at 932.6 and 952.5 eV can be observed (Fig. S9a). This is due

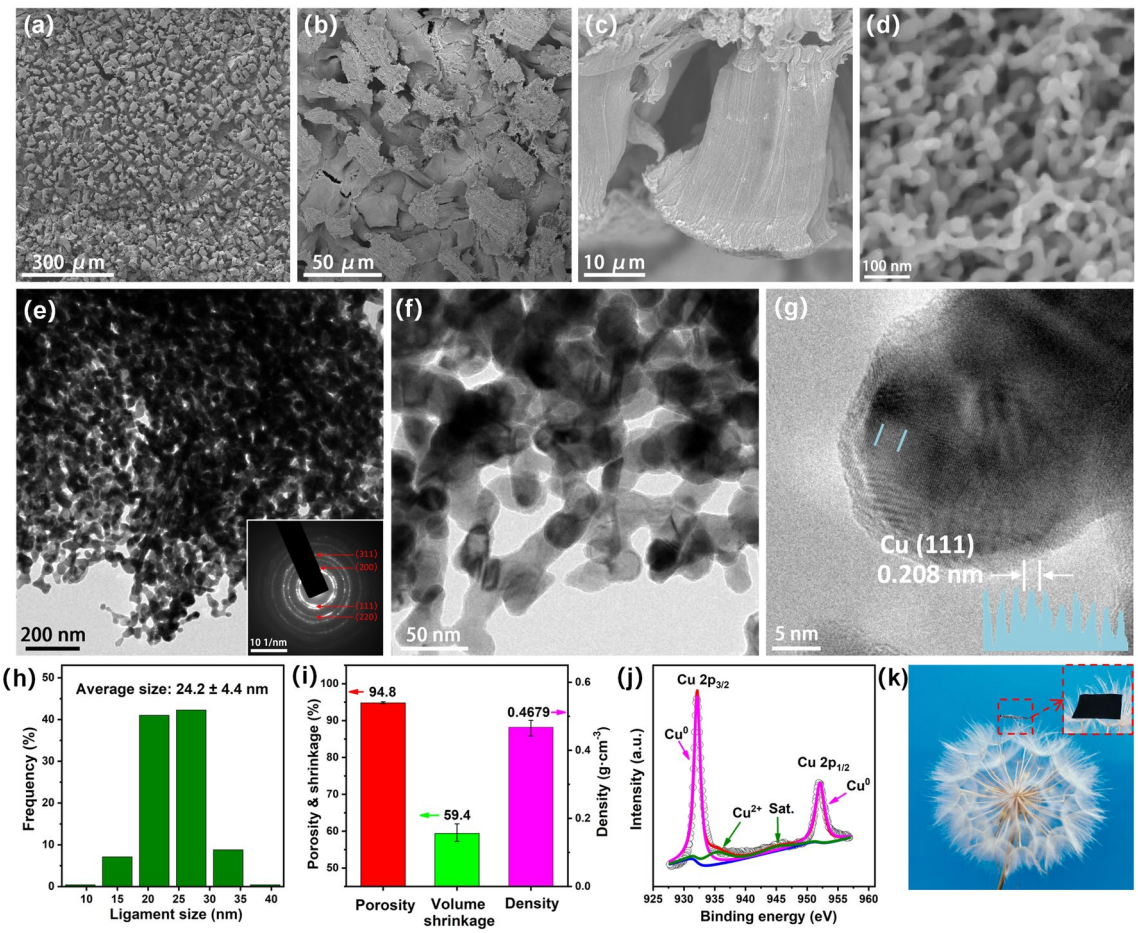

Fig. 4 **a–d** SEM images, **e**, **f** TEM images (Inset: SAED pattern), **g** HRTEM image, and **h** ligament size distribution of the NP-Cu film. **i** Summary of porosity, volume shrinkage and density, **j** XPS spectrum of Cu 2*p*, and **k** photograph of the NP-Cu film

to the extremely low Cu content in the dilute solid solution alloy. The XPS spectrum of Al 2*p* in Fig. S8b also confirms the minor residual of Al in the NP-Cu film in the state of Al^{3+} (Al_2O_3) [64]. In the $Al_{98}Cu_2$ precursor, the peaks of metallic state (Al^0) and oxidation state (Al^{3+}) of Al are located at 73.1 and 74.7 eV, respectively (Fig. S9b) [64]. In contrast, the peak intensity of Al^{3+} is higher, indicating that Al on the surface of the $Al_{98}Cu_2$ precursor is easy to be oxidized in air. The XPS spectrum of O 1*s* in Figure S8c shows two peaks at 530.2 and 531.9 eV in the NP-Cu film, corresponding to CuO [63] and Al_2O_3 [65, 66], respectively. Compared with the scenario of 3 and 10 min of dealloying, the relative peak intensity of CuO is further increased. This is the result of the thorough dealloying, which leads to a great decrease in Al content and a significant increase in Cu content. While in the $Al_{98}Cu_2$ precursor, only the peak associated with Al_2O_3 at 531.8 eV can be observed (Fig. S9c). Notably, dandelion fluff can support the NP-Cu film (Fig. 4k), which intuitively shows the advantages of light weight. Additionally, the NP-Cu-500 film is still composed of *f.c.c.* Cu, and the color changed from black to dark red and the size obviously shrank after annealing (Fig. S10a). The nanoporous structure coarsened to 47 ± 11 nm (Fig. S10b, c).

3.2 SSG Performance of NP-Cu Films

The SSG performance of the NP-Cu and NP-Cu-500 films was thus evaluated and the evaporator schematic is shown in Fig. 5a. The NP-Cu film can not only absorb sunlight and release heat through the LSPR effect, but also transport water through internal multi-scale channels. The PS foam with low thermal conductivity (0.04 W m^{-1} K^{-1}) can isolate the unnecessary heat exchange between the SSG system and the surrounding environment. Figure 5b–h shows the water evaporation performance of the NP-Cu film, with the NP-Cu-500 film as the benchmark. Infrared images (Fig. 5b) show the surface temperature distribution of the NP-Cu film under various illuminations and times. Regardless of the light intensity, the surface temperature of NP-Cu rapidly rises and remains stable thereafter. Figure 5c illustrates the time-dependent temperature changes. The surface temperature of NP-Cu increases sharply within 5 min and then reaches the plateau with slight temperature fluctuation under various illuminations. This phenomenon suggests that the NP-Cu film possesses good photothermal conversion capability. Specifically, the maximum surface temperatures of NP-Cu can reach up to 42.4, 62.3 and 71.6 °C under 1, 3 and 5 sun illumination, respectively. In comparison, the surface temperature of the NP-Cu-500 film can also increase rapidly and then keep a stable plateau of 39.1, 57.5 and 68.1 °C under 1, 3 and 5 sun illumination, respectively, lower than that of NP-Cu at the same illumination. This difference can be attributed to the fact that the smaller ligaments of NP-Cu can enrich more free electrons on the surface, thus enhancing the LSPR effect [67]. Figure 5d illustrates the mass change curves of the two films. The final mass changes of NP-Cu are 1.41, 4.31 and 7.18 kg m^{-2} under 1, 3 and 5 sun illumination respectively. Meanwhile, the mass changes of NP-Cu-500 are slightly smaller than those of NP-Cu under different illuminations. Figure 5e displays the curves of evaporation rate with time of NP-Cu. Apparently, the evaporation rate rises rapidly within 5 min and then remains stable. Figure 5f compares the evaporation rates of the NP-Cu and NP-Cu-500 films. The evaporation rate of NP-Cu is 1.47 kg m^{-2} h^{-1} under 1 sun illumination, slightly greater than that of NP-Cu-500 (1.43 kg m^{-2} h^{-1}). Under the light intensity (5 sun), the NP-Cu film shows the highest evaporation rate (7.47 kg m^{-2} h^{-1}), still higher than that of NP-Cu-500 (7.29 kg m^{-2} h^{-1}). The evaporation efficiency (η) was calculated by the following equation [68]:

$$\eta = \frac{\dot{m} h_{LV}}{I} \quad (1)$$

where $\dot{m}$ represents the evaporation rate in equilibrium, h_{LV} is the total enthalpy of liquid-vapor phase change (2260 kJ kg^{-1}) [69], I represents the power density of incident light. Figure 5g shows the evaporation efficiencies of the NP-Cu and NP-Cu-500 films. The evaporation efficiencies of the two films slightly fluctuate under different light intensities. The evaporation efficiencies of NP-Cu are 92.9%, 93.5% and 93.7% under 1, 3 and 5 sun illumination respectively, higher than those (89.6%, 90.6% and 91.6%) of NP-Cu-500. The evaporation efficiencies of NP-Cu and NP-Cu-500 films fluctuate little in 30 cycles (Figs. 5h and S11), indicating that the SSG system has good stability and durability. Moreover, there is no obvious change in the ligament size of NP-Cu after the cycling test (Fig. S12), suggesting the good structural stability of NP-Cu even under the irradiation of sunlight.

https://doi.org/10.1007/s40820-023-01063-z

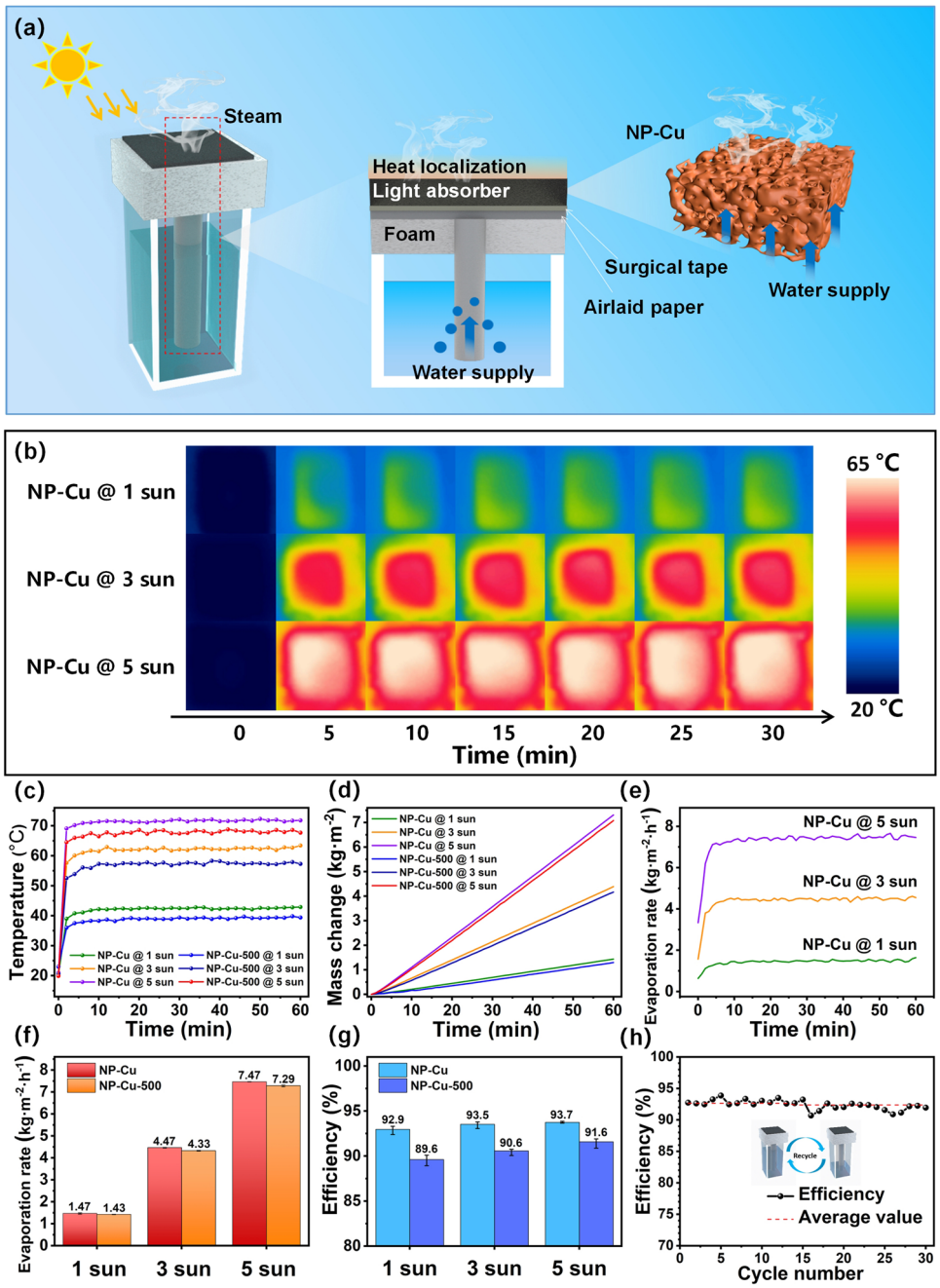

Fig. 5 **a** Schematic illustration of water evaporation process and mechanism. **b** Infrared images, **c** surface temperature changes, **d** mass changes, **e** evaporation rate with time, **f** evaporation rate and **g** evaporation efficiency of the NP-Cu and NP-Cu-500 films under different illuminations. **h** Cycling test of the NP-Cu film under 1 sun illumination

3.3 Seawater Desalination Property

In order to verify the seawater desalination performance of NP-Cu, a simple condensation recovery device was made for water purification (Fig. 6a). Water vapor escaping from the surface of the SSG system can condense on the inclined plane and then be collected. As observed in Fig. 6b, the ion concentration of Ca^{2+}, K^{+}, Mg^{2+} and Na^{+} in the seawater (Yellow Sea) decreases from 298.7, 307, 716, 6765 to 1.3, 2.9, 0.6, 9.9 mg L^{-1} respectively, which is noticeably

reduced after desalination and completely satisfies drinking water standards of the World Health Organization (WHO) [70]. Meanwhile, the NP-Cu film exhibits high ion rejections of more than 99.1% (Fig. 6c). Moreover, desalination experiments of different seawater (Bohai Sea and South China Sea) further prove the compatibility and adaptability of NP-Cu (Fig. 6d). These results jointly indicate the potential of the present NP-Cu film for seawater desalination applications. Similarly, the NP-Cu-500 film also shows good seawater desalination ability (Fig. S13). In order to study the influence of salt accumulation on the NP-Cu film, the seawater was used for solar evaporation cycle tests under 1 sun illumination. As shown in Fig. S14a, the evaporation efficiency of the NP-Cu film decreases slightly from 92.1% after 1 h of illumination to 87.9% after 7 h of illumination. The evaporation rate of the NP-Cu film has a similar downward trend. Obviously, compared with the initial state (Fig. S14b), salt accumulation appeared on the surface of the NP-Cu film after 7 h of illumination (Fig. S14c). The salt accumulation can block the porous structure of the surface, thus hinder water transfer and reduce light area, resulting in the decrease of the SSG performance of the NP-Cu film [71]. However, some salt crystals re-dissolved without illumination for 1 h (Fig. S14d), indicating the NP-Cu film has a certain anti-salt fouling ability.

3.4 Mechanism Analysis

The intrinsic mechanism of good SSG performance of NP-Cu was further explored. Excellent hydrophilicity is an important condition for efficient evaporation of photothermal materials [72, 73]. The contact angle will be affected by

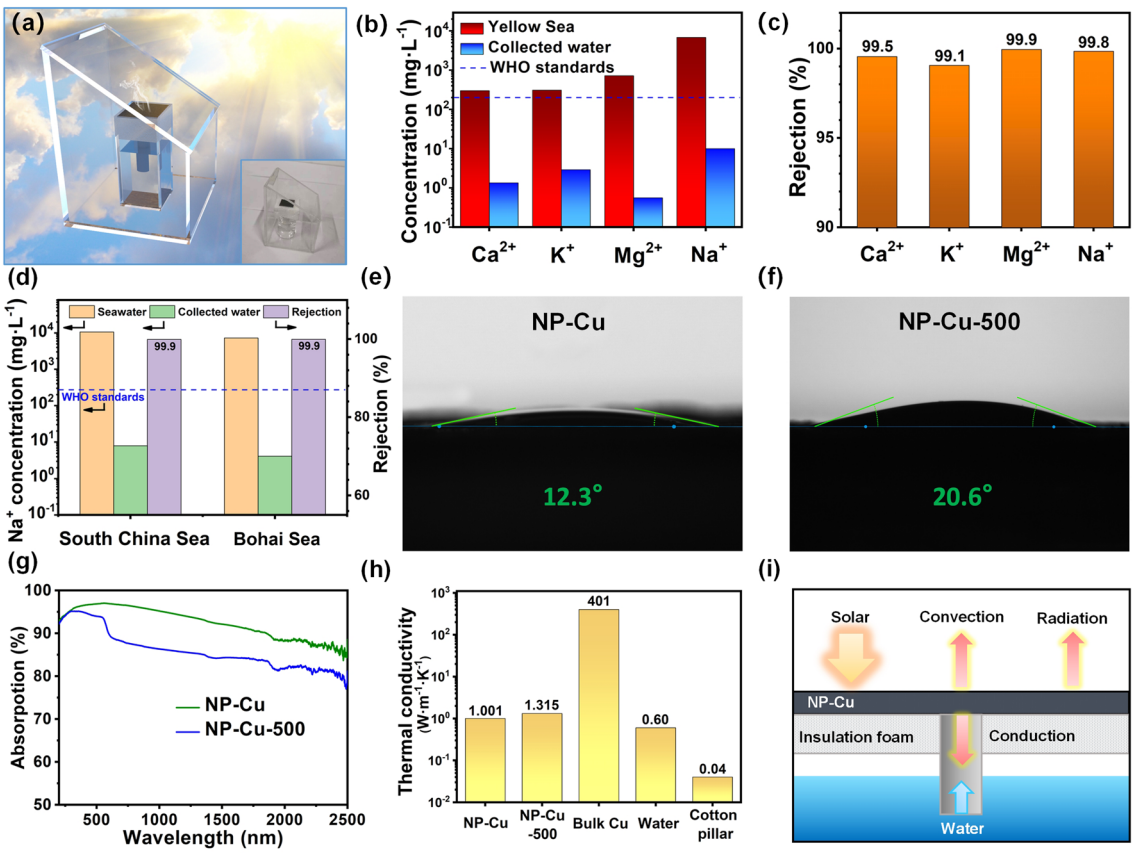

Fig. 6 **a** Schematic illustration of steam condensation recovery device. Inset: photograph of the device. **b** Concentrations of four metal ions in Yellow Sea and the collected clean water after desalination by the NP-Cu film. **c** Ion rejection of real seawater sample after desalination. **d** Na^+ concentrations in seawater (South China Sea and Bohai Sea) and the collected clean water after desalination by the NP-Cu film and corresponding rejection. **e**, **f** Contact angles of the **e** NP-Cu and **f** NP-Cu-500 films. **g** UV-vis-NIR absorption spectra of the NP-Cu and NP-Cu-500 films. **h** Summary of thermal conductivities for some related materials. **i** Schematic diagram of heat losses

 https://doi.org/10.1007/s40820-023-01063-z

the surface pore structure and its distribution [74]. The contact angles of NP-Cu and NP-Cu-500 are 12.3° and 20.6°, respectively (Fig. 6e, f), indicative of their excellent wettability and good water storage capacity. This means that water supply is not the key factor causing the difference of their SSG performance. To evaluate the light absorption capacity of the NP-Cu film and the NP-Cu-500 film, Fig. 6g shows the UV-vis-NIR spectra of NP-Cu and NP-Cu-500 in the wavelength range of 200–2500 nm. As seen in the whole spectra, the light absorption of NP-Cu is higher than that of NP-Cu-500. The high light absorption of NP-Cu-500 is mainly concentrated in the visible light region. In comparison, the NP-Cu film exhibits the good broadband absorption across the whole spectrum range. Especially in the wavelength range of 276–1039 nm, its absorption is more than 95%. The 3D bicontinuous ligament-channel structure as well as the fine ligaments (24.2 ± 4.4 nm) of NP-Cu is beneficial to increase the scattering path, thus enhancing light absorption [75]. Low thermal conductivity is a necessary condition for an ideal SSG system [26, 76], which can effectively reduce heat loss. The thermal conductivity of the NP-Cu film (1.001 W m^{-1} K^{-1}) or the NP-Cu-500 film (1.315 W m^{-1} K^{-1}) is much smaller than that of bulk Cu (401 W m^{-1} K^{-1}) and slightly larger than that of water (0.60 W m^{-1} K^{-1}) (Fig. 6h). The low thermal conductivity can efficiently localize the generated heat at the evaporation surface of the SSG system and avoid the rapid heat loss to the environment [77]. And the PS foam and cotton pillar with extremely low thermal conductivity (0.04 W m^{-1} K^{-1}) are beneficial to reduce the downward heat loss. Figure 6i reveals three main ways of heat loss, including conduction, convection and radiation [17, 78]. The heat conduction loss only accounts for 0.13% (Section S3), which further illustrates that the SSG system owns good thermal management and can make full use of heat to improve the evaporation efficiency.

Thus the excellent SSG performance of NP-Cu can be rationalized as follows. The unique 3D bicontinuous network structure of the NP-Cu film, coupled with multi-scale local structures (such as nano-ligaments and micro-channels), can effectively achieve broadband absorption of light [79–83]. The rough surface and the porous structure can enable multiple reflections, so as to improve light absorption. The generated steam can quickly escape from the porous structure of the NP-Cu film. Besides, the fine nano-ligament structure is beneficial to enhance the LSPR effect, thus achieving favorable photothermal conversion ability. The low thermal conductivity of each part of the SSG system contributes to realizing a stable heat concentration, limiting the converted heat to the photothermal layer and reducing heat loss. The good hydrophilicity makes the NP-Cu film have excellent water storage and delivery capability. Due to these good properties, the NP-Cu film possesses excellent SSG performance, coupled with low metal cost (Table S1), which has great development potentials as benchmarked with noble metals-based photothermal materials.

4 Conclusions

In summary, the self-supporting NP-Cu film with high porosity (94.8%) can be fabricated by one-step dealloying of the dilute solid $Al_{98}Cu_2$ precursor in the alkaline solution. The in-situ XRD and ex-situ SEM/XPS results well reveal the phase/microstructure/composition evolutions during the dealloying of $Al_{98}Cu_2$. The unique 3D network structure and multi-scale channels endow the NP-Cu film with good broadband absorption capability. The NP-Cu film exhibits excellent SSG performance (evaporation rate, efficiency and stability) and seawater desalination capability, which is associated with its broadband light absorption, enhanced LSPR effect by the nanoscale ligaments and good hydrophilicity. Due to the low price of Cu compared with precious metals like Au and Ag, this work provides a new approach to the design and fabrication of low-cost metal-based photothermal conversion materials for SSG systems.

Acknowledgements The authors gratefully acknowledge financial support by the Key Research and Development Program of Shandong Province (2021ZLGX01), the support of Taishan Scholar Foundation of Shandong Province, the Natural Science Foundation of Shandong Province (ZR2021QE229, ZR2022QB169), and the Postdoctoral Science foundation of China (2022M710077).

Funding Open access funding provided by Shanghai Jiao Tong University.

Supplementary Information The online version contains supplementary material available at https://doi.org/10.1007/s40820-023-01063-z.

References

1. S. Priyantha Ranjan, S. Kazama, M. Sawamoto, Effects of climate and land use changes on groundwater resources in coastal aquifers. J. Environ. Manag. **80**(1), 25–35 (2006). https://doi.org/10.1016/j.jenvman.2005.08.008
2. H. Li, Z. Yan, Y. Li, W. Hong, Latest development in salt removal from solar-driven interfacial saline water evaporators: advanced strategies and challenges. Water Res. **177**(15), 115770 (2020). https://doi.org/10.1016/j.watres.2020.115770
3. H. Wang, J. Zhao, Y. Li, Y. Cao, Z. Zhu et al., Aqueous two-phase interfacial assembly of COF membranes for water desalination. Nano-Micro Lett. **14**(1), 216 (2022). https://doi.org/10.1007/s40820-022-00968-5
4. W. Liu, K. Liu, H. Du, T. Zheng, N. Zhang et al., Cellulose nanopaper: fabrication, functionalization, and applications. Nano-Micro Lett. **14**(1), 104 (2022). https://doi.org/10.1007/s40820-022-00849-x
5. Y. Jiang, L. Chai, D. Zhang, F. Ouyang, X. Zhou et al., Facet-controlled $LiMn_2O_4$/C as deionization electrode with enhanced stability and high desalination performance. Nano-Micro Lett. **14**(1), 176 (2022). https://doi.org/10.1007/s40820-022-00897-3
6. X. Huang, L. Li, S. Zhao, L. Tong, Z. Li et al., MOF-like 3D graphene-based catalytic membrane fabricated by one-step laser scribing for robust water purification and green energy production. Nano-Micro Lett. **14**(1), 174 (2022). https://doi.org/10.1007/s40820-022-00923-4
7. C. Xu, Z. Yang, X. Zhang, M. Xia, H. Yan et al., Prussian blue analogues in aqueous batteries and desalination batteries. Nano-Micro Lett. **13**(1), 166 (2021). https://doi.org/10.1007/s40820-021-00700-9
8. S. Shen, J. Fu, J. Yi, L. Ma, F. Sheng et al., High-efficiency wastewater purification system based on coupled photoelectric-catalytic action provided by triboelectric nanogenerator. Nano-Micro Lett. **13**(1), 194 (2021). https://doi.org/10.1007/s40820-021-00695-3
9. R.M. Morris, The development of the multi-stage flash distillation process: a designer's viewpoint. Desalination **93**(1), 57–68 (1993). https://doi.org/10.1016/0011-9164(93)80096-6
10. I.G. Wenten, Khoiruddin, reverse osmosis applications: prospect and challenges. Desalination **391**, 112–125 (2016). https://doi.org/10.1016/j.desal.2015.12.011
11. C. Xu, J. Zhang, M. Shahriari-Khalaji, M. Gao, X. Yu et al., Fibrous aerogels for solar vapor generation. Front. Chem. **10**, 843070 (2022). https://doi.org/10.3389/fchem.2022.843070
12. A. Zhang, S. Zhao, L. Wang, X. Yang, Q. Zhao et al., Polycyclic aromatic hydrocarbons (PAHs) in seawater and sediments from the northern Liaodong Bay, China. Mar. Pollut. Bull. **113**(1), 592–599 (2016). https://doi.org/10.1016/j.marpolbul.2016.09.005
13. P. Zhang, J. Li, M.B. Chan-Park, Hierarchical porous carbon for high-performance capacitive desalination of brackish water. ACS Sustain. Chem. Eng. **8**(25), 9291–9300 (2020). https://doi.org/10.1021/acssuschemeng.0c00515
14. N.A.A. Qasem, S.M. Zubair, B.A. Qureshi, M.M. Generous, The impact of thermodynamic potentials on the design of electrodialysis desalination plants. Energy Convers. Manag. **205**, 112448 (2020). https://doi.org/10.1016/j.enconman.2019.112448
15. M. Gao, L. Zhu, C.K. Peh, G.W. Ho, Solar absorber material and system designs for photothermal water vaporization towards clean water and energy production. Energy Environ. Sci. **12**(3), 841–864 (2019). https://doi.org/10.1039/C8EE01146J
16. P. Tao, G. Ni, C. Song, W. Shang, J. Wu et al., Solar-driven interfacial evaporation. Nat. Energy **3**(12), 1031–1041 (2018). https://doi.org/10.1038/s41560-018-0260-7
17. J. Zhou, Y. Gu, P. Liu, P. Wang, L. Miao et al., Development and evolution of the system structure for highly efficient solar steam generation from zero to three dimensions. Adv. Funct. Mater. **29**(50), 1903255 (2019). https://doi.org/10.1002/adfm.201903255
18. T. Ding, Y. Zhou, W.L. Ong, G.W. Ho, Hybrid solar-driven interfacial evaporation systems: beyond water production towards high solar energy utilization. Mater. Today **42**, 178–191 (2021). https://doi.org/10.1016/j.mattod.2020.10.022
19. T. Ding, G.W. Ho, Using the sun to co-generate electricity and freshwater. Joule **5**(7), 1639–1641 (2021). https://doi.org/10.1016/j.joule.2021.06.021
20. D. Van-Duong, H.-S. Choi, Carbon-based sunlight absorbers in solar-driven steam generation devices. Glob. Chall. **2**(2), 1700094 (2018). https://doi.org/10.1002/gch2.201700094
21. J. Li, M. Du, G. Lv, L. Zhou, X. Li et al., Interfacial solar steam generation enables fast-responsive, energy-efficient, and low-cost off-grid sterilization. Adv. Mater. **30**(49), 1805159 (2018). https://doi.org/10.1002/adma.201805159
22. G. Chen, Z. Jiang, A. Li, X. Chen, Z. Ma et al., Cu-based MOF-derived porous carbon with highly efficient photothermal conversion performance for solar steam evaporation. J. Mater. Chem. A **9**(31), 16805–16813 (2021). https://doi.org/10.1039/D1TA03695E
23. D. Ding, H. Wu, X. He, F. Yang, C. Gao et al., A metal nanoparticle assembly with broadband absorption and suppressed thermal radiation for enhanced solar steam generation. J. Mater. Chem. A **9**(18), 11241–11247 (2021). https://doi.org/10.1039/d1ta01045j
24. M. Zhu, Y. Li, F. Chen, X. Zhu, J. Dai et al., Plasmonic wood for high-efficiency solar steam generation. Adv.

Energy Mater. **8**(4), 1701028 (2018). https://doi.org/10.1002/aenm.201701028

25. L. Zhang, J. Xing, X. Wen, J. Chai, S. Wang et al., Plasmonic heating from indium nanoparticles on a floating microporous membrane for enhanced solar seawater desalination. Nanoscale **9**(35), 12843–12849 (2017). https://doi.org/10.1039/c7nr05149b
26. Z. Guo, J. Wang, Y. Wang, J. Wang, J. Li et al., Achieving steam and electrical power from solar energy by MoS_2-based composites. Chem. Eng. J. **427**, 131008 (2022). https://doi.org/10.1016/j.cej.2021.131008
27. M.S. Irshad, X. Wang, M.S. Abbasi, N. Arshad, Z. Chen et al., Semiconductive, flexible MnO_2 NWs/chitosan hydrogels for efficient solar steam generation. ACS Sustain. Chem. Eng. **9**(10), 3887–3900 (2021). https://doi.org/10.1021/acssuschemeng.0c08981
28. X. Yang, Y. Yang, L. Fu, M. Zou, Z. Li et al., An ultrathin flexible 2D membrane based on single-walled nanotube–MoS_2 hybrid film for high-performance solar steam generation. Adv. Funct. Mater. **28**(3), 1704505 (2018). https://doi.org/10.1002/adfm.201704505
29. Y. Xu, H. Mu, X. Han, T. Sun, X. Fan et al., A simple, flexible, and porous polypyrrole-wax gourd evaporator with excellent light absorption for efficient solar steam generation. Int. J. Energy Res. **45**(15), 21476–21486 (2021). https://doi.org/10.1002/er.7195
30. Y. Zou, X. Chen, W. Guo, X. Liu, Y. Li, Flexible and robust polyaniline composites for highly efficient and durable solar desalination. ACS Appl. Energy Mater. **3**(3), 2634–2642 (2020). https://doi.org/10.1021/acsaem.9b02341
31. F. Wang, Y. Su, Y. Li, D. Wei, H. Sun et al., Salt-resistant photothermal materials based on monolithic porous ionic polymers for efficient solar steam generation. ACS Appl. Energy Mater. **3**(9), 8746–8754 (2020). https://doi.org/10.1021/acsaem.0c01292
32. P. Sun, W. Zhang, I. Zada, Y. Zhang, J. Gu et al., 3D-structured carbonized sunflower heads for improved energy efficiency in solar steam generation. ACS Appl. Mater. Interfaces **12**(2), 2171–2179 (2020). https://doi.org/10.1021/acsami.9b11738
33. J. Fang, J. Liu, J. Gu, Q. Liu, W. Zhang et al., Hierarchical porous carbonized lotus seedpods for highly efficient solar steam generation. Chem. Mater. **30**(18), 6217–6221 (2018). https://doi.org/10.1021/acs.chemmater.8b01702
34. N. Xu, X. Hu, W. Xu, X. Li, L. Zhou et al., Mushrooms as efficient solar steam-generation devices. Adv. Mater. **29**(28), 1606762 (2017). https://doi.org/10.1002/adma.201606762
35. Z. Lei, X. Sun, S. Zhu, K. Dong, X. Liu et al., Nature inspired MXene-decorated 3D honeycomb-fabric architectures toward efficient water desalination and salt harvesting. Nano-Micro Lett. **14**(1), 10 (2021). https://doi.org/10.1007/s40820-021-00748-7
36. H. Li, D. Jia, M. Ding, L. Zhou, K. Wang et al., Robust 3D graphene/cellulose nanocrystals hybrid lamella network for stable and highly efficient solar desalination. Sol. RRL **5**(8), 2100317 (2021). https://doi.org/10.1002/solr.202100317
37. J. Tian, X. Huang, W. Wu, Graphene-based stand-alone networks for efficient solar steam generation. Ind. Eng. Chem. Res. **59**(3), 1135–1141 (2020). https://doi.org/10.1021/acs.iecr.9b03523
38. Y. Yang, R. Zhao, T. Zhang, K. Zhao, P. Xiao et al., Graphene-based standalone solar energy converter for water desalination and purification. ACS Nano **12**(1), 829–835 (2018). https://doi.org/10.1021/acsnano.7b08196
39. Y. Zhang, Y. Wang, B. Yu, K. Yin, Z. Zhang, Hierarchically structured black gold film with ultrahigh porosity for solar steam generation. Adv. Mater. **34**(21), 2200108 (2022). https://doi.org/10.1002/adma.202200108
40. H. Wang, R. Zhang, D. Yuan, S. Xu, L. Wang, Gas foaming guided fabrication of 3D porous plasmonic nanoplatform with broadband absorption, tunable shape, excellent stability, and high photothermal efficiency for solar water purification. Adv. Funct. Mater. **30**(46), 2003995 (2020). https://doi.org/10.1002/adfm.202003995
41. Y. Yang, X. Yang, L. Fu, M. Zou, A. Cao et al., Two-dimensional flexible bilayer janus membrane for advanced photothermal water desalination. ACS Energy Lett. **3**(5), 1165–1171 (2018). https://doi.org/10.1021/acsenergylett.8b00433
42. B. Yu, Y. Wang, Y. Zhang, Z. Zhang, Nanoporous black silver film with high porosity for efficient solar steam generation. Nano Res. (2022). https://doi.org/10.1007/s12274-022-5068-x
43. C. Xiao, W. Liang, Q.-M. Hasi, L. Chen, J. He et al., Ag/polypyrrole co-modified poly(ionic liquid)s hydrogels as efficient solar generators for desalination. Mater. Today Energy **16**, 100417 (2020). https://doi.org/10.1016/j.mtener.2020.100417
44. A. Politano, P. Argurio, G. Di Profio, V. Sanna, A. Cupolillo et al., Photothermal membrane distillation for seawater desalination. Adv. Mater. **29**(2), 1603504 (2017). https://doi.org/10.1002/adma.201603504
45. M.M. Ghafurian, H. Niazmand, E.K. Goharshadi, B.B. Zahmatkesh, A.E. Moallemi et al., Enhanced solar desalination by delignified wood coated with bimetallic Fe/Pd nanoparticles. Desalination **493**, 114657 (2020). https://doi.org/10.1016/j.desal.2020.114657
46. Y. Fan, S. Wang, F. Wang, J. He, Z. Tian et al., The assembly of a polymer and metal nanoparticle coated glass capillary array for efficient solar desalination. J. Mater. Chem. A **8**(48), 25904–25912 (2020). https://doi.org/10.1039/D0TA08950H
47. M. Wang, P. Wang, J. Zhang, C. Li, Y. Jin, A ternary Pt/Au/TiO_2-decorated plasmonic wood carbon for high-efficiency interfacial solar steam generation and photodegradation of tetracycline. Chemsuschem **12**(2), 467–472 (2019). https://doi.org/10.1002/cssc.201802485
48. S. Kunwar, M. Sui, P. Pandey, Z. Gu, S. Pandit et al., Improved control on the morphology and LSPR properties of plasmonic Pt NPs through enhanced solid state dewetting by using a sacrificial indium layer. RSC Adv. **9**(4), 2231–2243 (2019). https://doi.org/10.1039/C8RA09049A

49. Z. Li, C. Wang, Novel advances in metal-based solar absorber for photothermal vapor generation. Chin. Chem. Lett. **31**(9), 2159–2166 (2020). https://doi.org/10.1016/j.cclet.2019.09.030
50. P. Wang, Emerging investigator series: the rise of nano-enabled photothermal materials for water evaporation and clean water production by sunlight. Environ. Sci. Nano **5**(5), 1078–1089 (2018). https://doi.org/10.1039/c8en00156a
51. F. Meng, B. Ju, S. Zhang, B. Tang, Nano/microstructured materials for solar-driven interfacial evaporators towards water purification. J. Mater. Chem. A **9**(24), 13746–13769 (2021). https://doi.org/10.1039/D1TA02202D
52. J. Yang, X. Suo, X. Chen, S. Cai, X. Ji et al., Water-light induced self-blacking system constituted by quinoa cellulose and graphene oxide for high performance of salt-rejecting solar desalination. Adv. Sustain. Syst. **6**(1), 2100350 (2022). https://doi.org/10.1002/adsu.202100350
53. I. McCue, E. Benn, B. Gaskey, J. Erlebacher, Dealloying and dealloyed materials. Annu. Rev. Mater. Res. **46**(1), 263–286 (2016). https://doi.org/10.1146/annurev-matsci-070115-031739
54. J. Erlebacher, M.J. Aziz, A. Karma, N. Dimitrov, K. Sieradzki, Evolution of nanoporosity in dealloying. Nature **410**(6827), 450–453 (2001). https://doi.org/10.1038/35068529
55. Z. Deng, J. Zhou, L. Miao, C. Liu, Y. Peng et al., The emergence of solar thermal utilization: solar-driven steam generation. J. Mater. Chem. A **5**(17), 7691–7709 (2017). https://doi.org/10.1039/c7ta01361b
56. F. Meng, Z. Ding, Z. Chen, K. Wang, X. Liu et al., N-doped carbon@Cu core–shell nanostructure with nearly full solar spectrum absorption and enhanced solar evaporation efficiency. J. Mater. Chem. A **10**(17), 9575–9581 (2022). https://doi.org/10.1039/D1TA10591D
57. S. Zhao, M. Xia, Y. Zhang, Q.-M. Hasi, J. Xu et al., Novel oil-repellent photothermal materials based on copper foam for efficient solar steam generation. Sol. Energy Mater. Sol. Cells **225**, 111058 (2021). https://doi.org/10.1016/j.solmat.2021.111058
58. Y. Wang, Q. Zhang, Y. Wang, L.V. Besteiro, Y. Liu et al., Ultrastable plasmonic Cu-based core–shell nanoparticles. Chem. Mater. **33**(2), 695–705 (2021). https://doi.org/10.1021/acs.chemmater.0c04059
59. X. Liu, Y. Tian, F. Chen, A. Caratenuto, J.A. DeGiorgis et al., An easy-to-fabricate 2.5D evaporator for efficient solar desalination. Adv. Funct. Mater. **31**(27), 2100911 (2021). https://doi.org/10.1002/adfm.202100911
60. N. Ponweiser, C.L. Lengauer, K.W. Richter, Re-investigation of phase equilibria in the system Al–Cu and structural analysis of the high-temperature phase η1-Al1−δCu. Intermetallics **19**(11), 1737–1746 (2011). https://doi.org/10.1016/j.intermet.2011.07.007
61. J.L. Murray, The aluminium-copper system. Int. Met. Rev. **30**(1), 211–234 (1985). https://doi.org/10.1179/imtr.1985.30.1.211
62. I. Najdovski, P.R. Selvakannan, S.K. Bhargava, A.P. O'Mullane, Formation of nanostructured porous Cu–Au surfaces: the influence of cationic sites on (electro)-catalysis. Nanoscale **4**(20), 6298–6306 (2012). https://doi.org/10.1039/C2NR31409F
63. M.F. Al-Kuhaili, Characterization of copper oxide thin films deposited by the thermal evaporation of cuprous oxide (Cu_2O). Vacuum **82**(6), 623–629 (2008). https://doi.org/10.1016/j.vacuum.2007.10.004
64. P. Motamedi, K. Cadien, XPS analysis of AlN thin films deposited by plasma enhanced atomic layer deposition. Appl. Surf. Sci. **315**, 104–109 (2014). https://doi.org/10.1016/j.apsusc.2014.07.105
65. N. Kumar, K. Biswas, Cryomilling: An environment friendly approach of preparation large quantity ultra refined pure aluminium nanoparticles. J. Mater. Res. Technol. **8**(1), 63–74 (2019). https://doi.org/10.1016/j.jmrt.2017.05.017
66. X. Li, H. Wu, G. Bin, W. Wu, D. Wu et al., Electrode-induced digital-to-analog resistive switching in TaOx-based RRAM devices. Nanotechnology **27**(30), 305201 (2016). https://doi.org/10.1088/0957-4484/27/30/305201
67. J. Liu, W. Shi, X. Wang, Cluster-nuclei coassembled into two-dimensional hybrid CuO-PMA sub-1 nm nanosheets. J. Am. Chem. Soc. **141**(47), 18754–18758 (2019). https://doi.org/10.1021/jacs.9b08818
68. M. Wang, J. Zhang, P. Wang, C. Li, X. Xu et al., Bifunctional plasmonic colloidosome/graphene oxide-based floating membranes for recyclable high-efficiency solar-driven clean water generation. Nano Res. **11**(7), 3854–3863 (2018). https://doi.org/10.1007/s12274-017-1959-7
69. M. Chen, Y. Wu, W. Song, Y. Mo, X. Lin et al., Plasmonic nanoparticle-embedded poly(p-phenylene benzobisoxazole) nanofibrous composite films for solar steam generation. Nanoscale **10**(13), 6186–6193 (2018). https://doi.org/10.1039/c8nr01017j
70. World Health Organization (WHO), *Safe drinking-water from desalination* (World Health Organization, Geneva, 2011)
71. C. Chen, Y. Kuang, L. Hu, Challenges and opportunities for solar evaporation. Joule **3**(3), 683–718 (2019). https://doi.org/10.1016/j.joule.2018.12.023
72. R. Li, C. Zhou, L. Yang, J. Li, G. Zhang et al., Multifunctional cotton with PANI-Ag NPs heterojunction for solar-driven water evaporation. J. Hazard. Mater. **424**, 127367 (2022). https://doi.org/10.1016/j.jhazmat.2021.127367
73. B. Yuan, C. Zhang, Y. Liang, L. Yang, H. Yang et al., Defect-induced self-cleaning solar absorber with full-spectrum light absorption for efficient dye wastewater purification. Sol. RRL **5**(5), 2100105 (2021). https://doi.org/10.1002/solr.202100105
74. S. Wang, Y. Fan, F. Wang, Y. Su, X. Zhou et al., Potentially scalable fabrication of salt-rejection evaporator based on electrogenerated polypyrrole-coated nickel foam for efficient solar steam generation. Desalination **505**, 114982 (2021). https://doi.org/10.1016/j.desal.2021.114982
75. S. Ai, M. Ma, Y.-Z. Chen, X.-H. Gao, G. Liu, Metal-ceramic carbide integrated solar-driven evaporation device based on ZrC nanoparticles for water evaporation and desalination. Chem. Eng. J. **429**, 132014 (2022). https://doi.org/10.1016/j.cej.2021.132014

 https://doi.org/10.1007/s40820-023-01063-z

76. Y. Liu, S. Yu, R. Feng, A. Bernard, Y. Liu et al., A bioinspired, reusable, paper-based system for high-performance large-scale evaporation. Adv. Mater. **27**(17), 2768–2774 (2015). https://doi.org/10.1002/adma.201500135
77. A. Ebrahimi, E.K. Goharshadi, M. Mohammadi, Reduced graphene oxide/silver/wood as a salt-resistant photoabsorber in solar steam generation and a strong antibacterial agent. Mater. Chem. Phys. **275**, 125258 (2022). https://doi.org/10.1016/j.matchemphys.2021.125258
78. Z. Deng, P.-F. Liu, J. Zhou, L. Miao, Y. Peng et al., A novel ink-stained paper for solar heavy metal treatment and desalination. Sol. RRL **2**(10), 1800073 (2018). https://doi.org/10.1002/solr.201800073
79. P. Qiao, J. Wu, H. Li, Y. Xu, L. Ren et al., Plasmon Ag-promoted solar–thermal conversion on floating carbon cloth for seawater desalination and sewage disposal. ACS Appl. Mater. Interfaces **11**(7), 7066–7073 (2019). https://doi.org/10.1021/acsami.8b20665
80. Y. Liu, Z. Liu, Q. Huang, X. Liang, X. Zhou et al., A high-absorption and self-driven salt-resistant black gold nanoparticle-deposited sponge for highly efficient, salt-free, and long-term durable solar desalination. J. Mater. Chem. A **7**(6), 2581–2588 (2019). https://doi.org/10.1039/C8TA10227A
81. L. Zhou, Y. Tan, D. Ji, B. Zhu, P. Zhang et al., Self-assembly of highly efficient, broadband plasmonic absorbers for solar steam generation. Sci. Adv. **2**(4), e1501227 (2016). https://doi.org/10.1126/sciadv.1501227
82. K. Bae, G. Kang, S.K. Cho, W. Park, K. Kim et al., Flexible thin-film black gold membranes with ultrabroadband plasmonic nanofocusing for efficient solar vapour generation. Nat. Commun. **6**, 10103 (2015). https://doi.org/10.1038/ncomms10103
83. D. Jalas, R. Canchi, A.Y. Petrov, S. Lang, L. Shao et al., Effective medium model for the spectral properties of nanoporous gold in the visible. Appl. Phys. Lett. **105**(24), 241906 (2014). https://doi.org/10.1063/1.4904714